Microwave spectroscopy of positronium atoms in free space

R. E. Sheldon, T. J. Babij, S. H. Reeder, S. D. Hogan, and D. B. Cassidy

Department of Physics and Astronomy, University College London, Gower Street, London WC1E 6BT, England, United Kingdom

We report measurements of the positronium (Ps) $2\,^3S_1 \rightarrow 2\,^3P_2$ interval in which atoms traveling in free space were irradiated with microwave radiation generated using a horn antenna. Previous measurements of this transition, performed using atoms in waveguides, exhibited asymmetric and shifted line shapes. In the free-space measurements we report here, much smaller line-shape asymmetry was observed, but with large frequency shifts that varied with the orientation of the horn antenna. Our observations are supported by line-shape simulations and demonstrate that variations in the microwave radiation field distribution can perturb measured line shapes and give rise to apparent frequency shifts without necessarily causing large asymmetries; this effect can explain previous measurements in which an apparent discrepancy with predictions from quantum electrodynamics was observed [L. Gurung, T. J. Babij, S. D. Hogan, and D. B. Cassidy, Phys. Rev. Lett. **125**, 073002 (2020)].

I. INTRODUCTION

As it is composed only of leptons and has no nuclear structure, positronium (Ps) [1] is a useful system with which to test bound-state QED theory [2,3]. This can be accomplished by performing precision laser or microwave spectroscopy of Ps energy levels [4–10], and comparing the results to calculations, which have been completed up to $O(m\alpha^6)$ (e.g., [11,12] and references therein), as well as some higher-order terms (e.g., [13,14]).

Historically, microwave spectroscopy has been used to study the properties of atoms and molecules; well-defined sources of microwave radiation [15] made it possible to perform precision spectroscopy [16], and even after the invention of the "optical maser" (or laser) [17], microwave spectroscopy has remained a valuable tool for atomic and molecular physics [18]. For example, microwave spectroscopy of the fine structure in hydrogen revealed an unexpected energy difference between the $2^2 S_{1/2}$ and $2\,^2P_{1/2}$ levels [19]. This energy interval, now known as the Lamb shift, was found to be ≈ 1 GHz, and its explanation required the development of quantum electrodynamics [20]. Since then microwave methods have been extensively used to study the hydrogen fine structure (e.g., [21–25]). These measurements have increasingly employed new experimental techniques, such as the Ramsey method of separated oscillatory fields [26].

Positronium studies with microwaves have been limited to measurements of the ground-state hyperfine interval [7] and the $n = 2$ fine structure [6,8,9], which is the subject of the present paper. Current experimental results are far less precise than calculated energy intervals in Ps [3]. In particular, the $n = 2$ fine-structure intervals, $2\,^3S_1 \rightarrow 2\,^3P_J$ ($J = 0, 1, 2$),

have been calculated with an estimated uncertainty of 80 kHz, while experimental uncertainties are in the few-MHz range. Recent measurements of these intervals (henceforth denoted by ν_J) have yielded improved precision (sub-MHz), but have also revealed a discrepancy with theory for the ν_0 transition [10], as well as asymmetric line shapes for the ν_1 and ν_2 transitions [27].

The observed ν_0 shift of 2.77 MHz [10] amounts to a more than 4σ discrepancy with theory. The asymmetric line shapes observed for the ν_1 and ν_2 transitions [27] also indicated shifts on the order of a few MHz, but in the absence of a line-shape model that could properly account for the asymmetries it was not possible to determine the resonance frequencies from these measurements, and consequently if there was agreement with theory or not.

Subsequent numerical investigations [28] showed conclusively that these observations could not be explained by quantum interference (QI) effects. A full density-matrix analysis of the quantum dynamics of the system determined that QI effects would indeed be present, but that they will only lead to line-shape distortions corresponding to shifts on the order of 100 kHz. It was found, however, that microwave reflections could possibly explain the observations; the microwave radiation fields in the experimental apparatus were simulated using numerical finite element methods (FEMs). frequency-dependent power variations within the waveguides used in the experiments were found to arise from radiation reflected from the vacuum chamber walls [28]. This has the effect that the power in the waveguide is not constant across the frequency range of the transition, and can therefore result in asymmetric line shapes. Our simulations also indicated that the same effect can cause *apparent* shifts, even if the measured line shapes do not appear to be asymmetric.

Here we exlplore these effects through a different kind of measurement; instead of driving transitions in Ps atoms as they pass through a waveguide, as was done in the previous work, a horn antenna was used to irradiate atoms with microwave radiation in free space. We find that, while it is

possible in this approach to obtain symmetric line shapes, and to avoid transit time broadening, we nevertheless still observe significant shifts of the ν_2 transition frequency. Moreover, these shifts strongly depend on the orientation of the horn antenna. As discussed below, this can be attributed to complex microwave radiation field distributions arising from reflections or interference in the vacuum chamber. Our observations support the conclusions obtained from previous simulations [28], namely that line shapes can appear to be shifted through this mechanism without exhibiting measurably asymmetric line shapes. This effect can explain the previously observed discrepancy [10].

II. EXPERIMENTAL METHODS

A. Ps production and excitation

The positron beam and Ps production and detection methods used in the experiments we report here have been described in detail elsewhere [29,30]. Briefly, β^+ particles emitted from a ^{22}Na source were moderated using a solid neon moderator [31] to produce a monoenergetic positron beam which was magnetically guided to a two-stage Surko-type buffer gas trap [32]. The trap generated pulses containing at least 10^5 positrons with a Gaussian spatial profile with a full width at half maximum (FWHM) of 3 mm, at a 1-Hz repetition rate. The positron pulses were compressed temporally using a harmonic buncher [33] to a FWHM of 3 ns and implanted into a mesoporous silica film [34] to produce ground-state Ps atoms. The target electrode (labeled T in Fig. 1) upon which the silica film was mounted was biased to -3.5 kV during positron implantation to optimize Ps production and cooling, allowing us to obtain Ps formation efficiencies on the order of 25% and transverse Ps energies of ≈ 50 meV [35].

Following positron implantation, Ps atoms were emitted from the silica film surface (within 10 ns [36]) into the space between the target (T) and grid (G) electrodes (see Fig. 1), which we refer to as the laser excitation region (LER). The spacing between the T and G electrodes was 11.5 mm, meaning that with $V_T = -3.5$ kV and $V_G = 0$ V, the electric field in the LER was ≈ 3 kV/cm. In this field $1\,^3S_1 \rightarrow 2\,^3P_J$ transitions were driven using a pulsed ultraviolet dye laser ($\lambda = 243.01$ nm, $\Delta\nu = 100$ GHz, $\Delta t = 4$ ns [29]). The strong electric field in the LER results in the production of mixed $n = 2$ states containing both $2\,^3S_1$ and $2\,^3P_J$ character [37]. Immediately after laser excitation, V_T was switched to 0 V in < 25 ns, allowing the mixed state atoms to evolve adiabatically into pure $2\,^3S_1$ states in zero electric field (see [38] for details). The grid electrode (G) contains a high transmission (95%) tungsten mesh.

We refer to the space outside the LER as the microwave excitation region (MER). To ensure that only events in the MER contributed to the microwave signal, the microwave radiation was turned on at $t_\mu = 510$ ns after the positron beam implantation. This delay allowed virtually all Ps atoms to exit the LER, and for V_T to be switched to 0 V before any microwave transitions could occur.

Microwave radiation was produced by a signal generator (Keysight N5173B) and amplified using a low noise amplifier
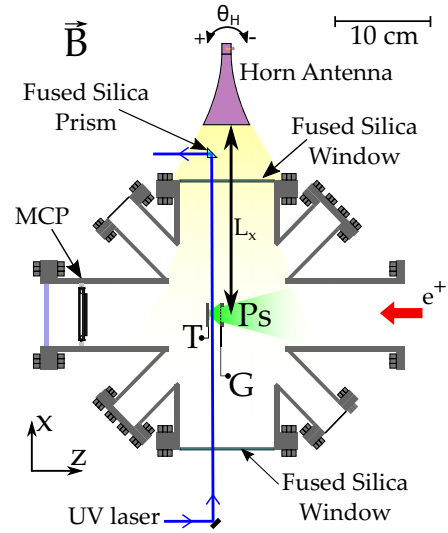

FIG. 1. Schematic representation of the experimental target chamber. A pulsed positron beam (red arrow) is implanted into a silica target to generate Ps atoms. These are excited to the $2\,^3S_1$ level (green cone) by a UV laser propagating in the $+x$ direction. The laser passes through the target (T) and grid (G) electrodes, and is deflected away from the horn antenna (purple cone) by a fused silica prism as indicated. The microwave radiation (yellow shading) propagates in the $-x$ direction. L_x represents the distance from the front of the horn antenna to the center of the chamber. The upstream MCP was used to monitor the positron beam size, position, and temporal width. The experiments were conducted in an axial magnetic field orientated along the z axis with a field strength of ≈ 32 G.

(Microwave Amps AL7). Free-space radiation was generated using a WR-102 standard gain horn antenna with a nominal 15-dB gain (Pasternack PE9857/SF-15). The antenna was arranged such that radiation propagated in the $-x$ direction and entered the vacuum system through a fused silica vacuum window, as shown in Fig. 1. To prevent UV light (traveling in the $+x$ direction) from striking the antenna, the laser beam was deflected by a fused silica prism mounted on a plastic rod.

Frequency-dependent variations in the microwave power at the horn antenna input (P_{input}) were measured using a power meter (Keysight N1913A and U8487A power sensor) and stabilized to within 0.01 dB m. However, the gain of the horn antenna is frequency dependent and can be expected to vary linearly by ≈ 1 dBm over the range of the measurement. This was not explicitly taken into account in the power stabilization; CST simulations show that the frequency variations of the effective gain, as measured by the average microwave power in the vacuum chamber, are greater than the intrinsic antenna gain variations.

The antenna output consists of radiation emitted in a cone with 50% of the emitted power contained within an angular spread of 29.6°, as specified by the manufacturer. The radiation was polarized along the short axis of the antenna, which is in the z dimension, parallel to the applied magnetic field. From the exit of the antenna up to a distance d_{rad}, radiation propagated in the near-field regime, meaning that the $\vec{E}$ and $\vec{H}$ components of the field are out of phase and not orthogonal to the direction of travel. Distances greater than d_{rad}

constitute the far-field regime, in which radiation propagates as plane waves, with the direction of motion of the Ps atoms perpendicular to the electric and magnetic components of the field. For a horn antenna this distance is given by (e.g., [39]) $d_{\rm rad} = 2D^2/\lambda$, where D is the largest dimension of the antenna output and λ is the wavelength of the radiation.

In the present case $D = 6.86$ cm and $\nu = 8.6267\,1$ GHz is the frequency of the $2\,^3S_1 \rightarrow 2\,^3P_2$ transition. Thus, $\lambda = 3.57$ cm, and $d_{\rm rad} \approx 26$ cm. Measurements were performed in both the near- and far-field regimes, with the horn antenna located at $L_x = 21$ cm and 34 cm from the center of the vacuum chamber (see Fig. 1). However, the distinction between these regimes is largely irrelevant in the present case owing to the reflections of the radiation in the vacuum chamber, as discussed in Sec. III A.

The horn antenna was mounted on a rotation stage so that the angle between the antenna axis and the x axis, θ_H, could be varied, with measurements performed for different values of θ_H. We note that the $\theta_H = 0°$ position is not necessarily perfectly aligned with the x axis, and is subject to some uncertainty, which we estimate to be $\pm 2°$.

B. Line-shape fitting

Ps annihilation lifetime spectra were recorded via a single-shot lifetime spectroscopy method [40] using three gamma ray detectors, each comprising a lutetium-yttrium oxyorthosilicate scintillator attached to a photomultiplier tube [41]. Lifetime spectra were integrated over selected time windows (AC and AB) to obtain f_{AB} and f_{AC}. These were used to generate the parameter f_d according to

$$f_d = \frac{f_{AC} - f_{AB}}{f_{AC}}, \tag{1}$$

where the times t_B and t_C were set independently for each detector to optimize the signal-to-noise ratio; typical values were 700 and 1400 ns, respectively. Time t_A refers to the beginning of the measurement cycle (-30 ns) and $t = 0$ corresponds to the time at which the positron pulse was implanted into the silica target (see [27] for details). This parameter was measured with ($f_{\rm on}$) and without ($f_{\rm off}$) microwave radiation present, and the effect of the radiation was quantified using the signal parameter S_γ, defined as

$$S_\gamma = \frac{f_{\rm off} - f_{\rm on}}{f_{\rm off}}. \tag{2}$$

Spectral line shapes were then generated by measuring S_γ as a function of the microwave frequency. Figure 2 shows an example of a line shape measured in this way for $\theta_H = 0°$, $L_x = 21$ cm, and $P_{\rm input} = 94$ mW. The data were fitted using a Lorentzian function of the form

$$L(\nu) = \frac{2A/\pi\,\Gamma}{1 + 4[(\nu - \nu_R)/\Gamma]^2}, \tag{3}$$

where A is a constant, Γ is the width (FWHM), and ν_R is the resonance frequency of the transition. Note that ν_R differs from the resonance frequency ν_2 in the presence of a magnetic field because of the Zeeman effect [42].

In previous measurements, the ν_2 line shapes were found to be asymmetric [27], and the asymmetry was empirically
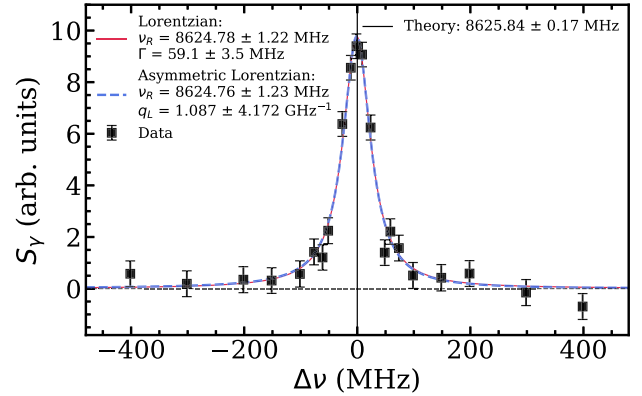

FIG. 2. An example of a line shape measured using $L_x = 21$ cm, $P_{\rm input} = 94$ mW, and $\theta_H = 0°$. The data are fitted using Lorentzian (solid red) and asymmetric Lorentzian (blue dashed) functions, with corresponding fit parameters shown in the legends. The solid vertical line at $\Delta\nu = 0$ corresponds to the Zeeman shifted theoretical transition frequency 8625.84 MHz. The data were recorded in a magnetic field of ≈ 32 G.

characterized using a Fano function [43]. This function has an asymmetry parameter q that can have positive or negative values, depending on the direction of the line-shape asymmetry, and it is possible to obtain stable fits for both positive and negative values. For highly asymmetric line shapes it is usually obvious which solution best fits the data (for example, as indicated by the $\chi^2_{\rm red}$ value), but this is not necessarily the case for symmetric or nearly symmetric lines. Therefore, in the present paper we use a different asymmetric fitting function to characterize asymmetry, namely a modified asymmetric Lorentz function, in which the width parameter is replaced with $\Gamma_A(\nu)$, a sigmoidally varying frequency-dependent function of the form [44]

$$\Gamma_A(\nu) = \frac{2\Gamma}{1 + \exp[q_L(\nu - \nu_R)]}, \tag{4}$$

where q_L is the asymmetry parameter. In the limit $q_L \rightarrow 0$ the asymmetric Lorentz function [Eq. (4)] approaches a Lorentzian function.

As discussed in Sec. IV, most of the data recorded in the present experiments did not show any significant asymmetry insofar as (i) the average q_L values were all consistent with nearly symmetric lines and (ii) the obtained centroid values for both symmetric and asymmetric fitting were always consistent within the fit uncertainties. The results presented henceforth are therefore based on Lorentzian fits.

III. SIMULATIONS

A. Microwave FEM simulations

In order to better understand the atom-radiation interactions in the experiment, numerical simulations of the microwave fields expected in the apparatus were obtained using CST Studio Suite software [45]. This software evaluates three-dimensional electromagnetic fields using a FEM, and can be used to calculate the phase and magnitude of the
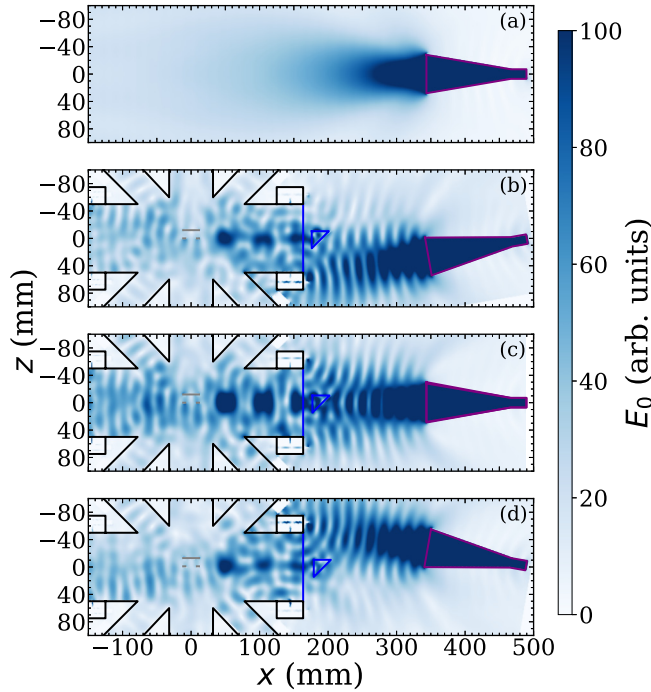
FIG. 3. FEM simulations of the spatial distribution of the magnitude of the electric-field component E_0 of 8.626 71 GHz microwave radiation in (a) free space and (b)–(d) the experimental vacuum chamber with a horn antenna angle $\theta_H = -10°$, $0°$, and $+10°$, respectively.

FIG. 4. Monte Carlo simulations of the location of microwave induced $2\,^3S_1 \rightarrow 2\,^3P_2$ transitions (green squares), self-annihilation events (blue triangles), and collisions of Ps atoms (red circles) in (a) the xz plane and (b) the yz plane. Solid black lines denote solid metal objects, namely, the target and grid electrodes and the vacuum chamber. The color map shows the magnetic-field strength in and around the vacuum chamber.

electromagnetic field using a time domain solver (see [28] for more details).

The free-space radiation field obtained from the simulations is shown in Fig. 3(a); the corresponding case including the experimental apparatus is shown in Figs. 3(b)–3(d) for different antenna angles θ_H.

The simulation layout was designed to match that of the experiment, and the CST materials library was used to appropriately model individual components of the apparatus. It can be seen from the difference between the simulations of free space and the experimental analog that interference due to reflected radiation causes a highly anisotropic field distribution in the chamber. Additionally, asymmetric components such as the prism and T and G electrodes cause different radiation patterns dependent on the value of θ_H.

Atoms moving toward the horn in the $+x$ direction will be preferentially excited due to larger field intensity near the source of the radiation. However, as indicated in Fig. 4, the Ps velocities in the x direction are limited by laser velocity selection and this is not expected to result in any measurable effect.

B. Particle trajectory simulations

Simulations of $2\,^3S_1$-atom trajectories were performed in order to estimate where and how atoms were likely to decay. The velocity distributions of the emitted atoms were the same as those shown in Fig. 2 of [28]. These are based on measured ground-state distributions, and the velocity selection in the x direction arising from the 100-GHz bandwidth of the UV
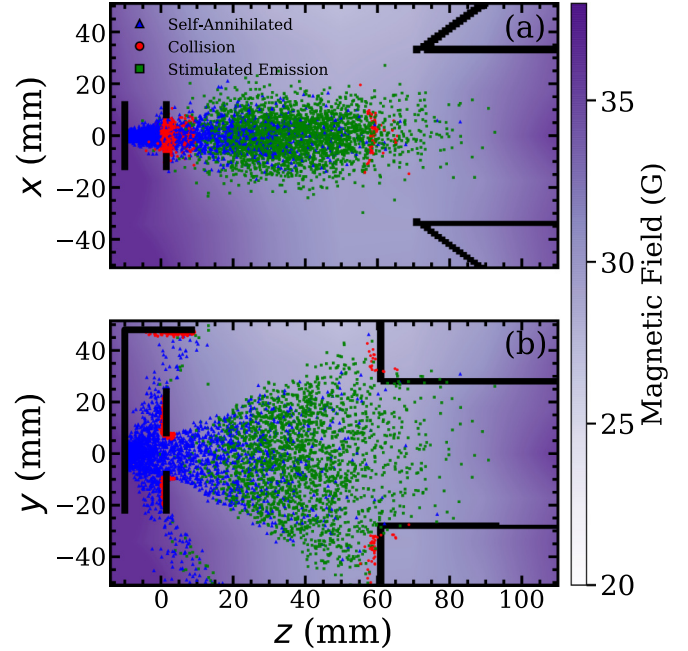
excitation laser. In the simulations, long-lived $2\,^3S_1$ atoms produced annihilation γ rays through one of three channels: (1) collisions with electrodes or the internal surfaces of the vacuum chamber ($2\,^3S_1 + X \rightarrow 2\gamma$), (2) direct self-annihilation ($2\,^3S_1 \rightarrow 3\gamma$), or (3) microwave driven stimulated emission ($2\,^3S_1 \rightarrow 2\,^3P_2 \rightarrow 1\,^3S_1 \rightarrow 3\gamma$). The decay channel for each atom was determined via a Monte Carlo selection, taking into account the particle position, decay rate, and time since creation. The results of the simulations are shown in Fig. 4.

Collisions with material objects, such as electrodes or the chamber walls, are likely to result in direct two-photon annihilation with electrons external to the Ps atoms (i.e., pickoff annihilation [46]). In some cases slow Ps atoms may reflect from clean surfaces (e.g., [47]) but in the present case this process was expected to be negligible and was not included in the simulations. Self-annihilation occurs with a mean lifetime of 1120 ns in the 32-G magnetic field [37], with the lifetime of each simulated atom randomly sampled from an exponential distribution derived from the appropriate Zeeman shifted decay rate. In the simulations, all microwave transitions occurred immediately after the radiation was turned on at time t_μ (see Sec. II A), simulating saturation. The typical distribution of locations of the atoms when the $2\,^3S_1 \rightarrow 2\,^3P_2$ transitions occurred is shown in Fig. 4. However, the annihilation radiation is not emitted until the subsequent $2\,^3P_2 \rightarrow 1\,^3S_1 \rightarrow 3\gamma$ decay. Since the $2\,^3P_2 \rightarrow 1\,^3S_1$ radiative decay is fast (the mean lifetime is 3.2 ns) this process will have a mean decay time constant of 142 ns, dominated by the ground-state decay rate; during this time the atoms may travel ≈ 1 cm. Thus, the real

spatial distributions of the annihilation events will be slightly more spread out than shown in Fig. 4.

The color map in Fig. 4 represents variations in the magnetic field in the MER, determined by measurements using a duplicate coil arrangement. The average magnetic field in the MER experienced by atoms upon application of the microwave radiation was 32.0 ± 2.1 G. This will cause an average Zeeman shift of -0.87 ± 0.13 MHz [37]. All data presented here were recorded in this magnetic field.

C. Line-shape modeling

To investigate the effects of inhomogeneities in the microwave field distribution on the spectral line shapes and measured resonance frequencies, numerical calculations were performed that accounted for trajectories of atoms in these fields and the time evolution of the population of the $2\,^3S_1$ and $2\,^3P_2$ levels. For simplicity, these calculations were restricted to treating the $\Delta M_J = 0$ transition between sublevels with $M_J = 0$, i.e., the $2\,^3S_1(0) \rightarrow 2\,^3P_2(0)$ transition, where the numbers in brackets represent the value of M_J. This transition has an electric dipole transition moment of $\approx 5ea_0$, where e is the electronic charge and a_0 is the Bohr radius [27].

Detailed modeling of the quantum dynamics in Ps microwave spectroscopy was performed in [28]. In that work 20 real quantum states were included (16 with $n = 2$ and 4 with $n = 1$) as well as some fictitious annihilation vacuum states. This resulted in more than 400 coupled differential equations, and clearly revealed the extent to which quantum interference effects can contribute to our signal. Based on this, we find that the system can be adequately described using a simplified approach.

The calculations associated with the work reported here were performed by solving the Lindblad master equation [48,49] for a model four-level system using the open-source PYTHON framework QUTIP [50,51]. This model system comprised the initial $2\,^3S_1(0)$ sublevel that decayed at the (Zeeman corrected) rate $\gamma_{2S} = (1120\,\text{ns})^{-1}$ to a discrete far-detuned state representing the vacuum. Also included were the $2\,^3P_2(0)$ sublevel to which the microwave transition was driven, and the $1\,^3S_1$ ground level. The (Zeeman shifted [27]) $2\,^3S_1(0)$ and $2\,^3P_2$ sublevels were coupled by the microwave driving field at a resonant Rabi frequency $\Omega_{2S_1(0),\,2P_2(0)}(t)$. The short-lived $2\,^3P_2(0)$ sublevel decayed by spontaneous emission at a rate $\gamma_{2P} = (3.2\,\text{ns})^{-1}$ to the ground level. In the calculations, all population initially resided in the $2\,^3S_1(0)$ sublevel. The time dependence of the microwave field, and hence $\Omega_{2S_1(0),\,2P_2(0)}(t)$, for each individual atom along its trajectory from the excitation region was obtained from the particle trajectory and FEM simulations described above. This time-dependent Rabi frequency was used as the input into the calculation of the time evolution of the internal-state populations.

For each atom (or trajectory) considered in the calculations, the microwave field distribution was obtained for microwave frequencies ranging from 8200 to 9000 MHz, matching those used in the experiments. As an example, Fig. 5 shows the result obtained for an individual trajectory along the z axis of the apparatus at $(x, y) = (0, 0)$ and a frequency of 8624.38 MHz. The horizontal axis represents the time after
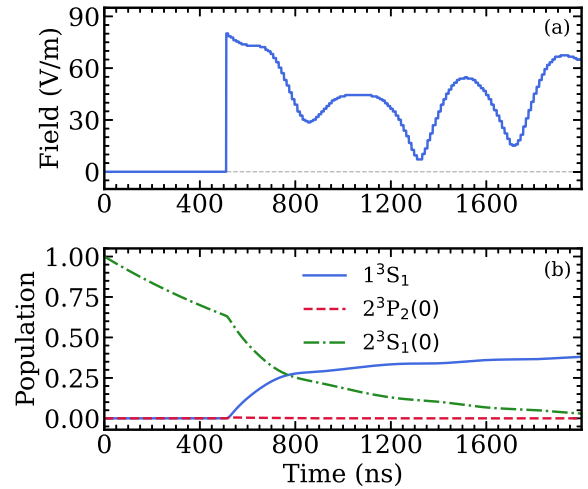

FIG. 5. (a) Typical calculated time dependence of the amplitude of a 8624.38-MHz microwave field experienced by an atom propagating along the z axis of the apparatus at $(x, y) = (0, 0)$. (b) Calculated time evolution of the internal-state populations for an atom initially in the $2\,^3S_1(0)$ level upon interaction with the field in (a).

excitation to the $2\,^3S_1$ level. Figure 5(a) shows the amplitude of the microwave field experienced by the atom as it propagates along its trajectory. The abrupt onset of the field at 510 ns reflects the delay time between photoexcitation and the activation of the microwave pulse in the experiments. This delay was implemented to ensure that atoms were only addressed by microwave radiation in the MER, as discussed in Sec. II A. The discrete variations in field amplitude data arise from converting the spatial resolution of the CST field calculation into the time domain for a particular trajectory. As a test these data were smoothed to generate a continuous field distribution but no change in the results of the simulations was observed. As can be seen from the figure, the field experienced by the atom as it follows this trajectory varies by almost an order of magnitude between different positions along the path (see Fig. 3). This variation in field strength is both frequency and position dependent, and as a result can affect the measured and simulated spectral line shapes.

The calculated time dependence of the populations of the $2\,^3S_1(0)$, $2\,^3P_2(0)$ and $1\,^3S_1$ levels in the microwave field in Fig. 5(a) is shown in Fig. 5(b). At early times, i.e., before 510 ns, the $2\,^3S_1$ level (dash-dotted green curve) decays by self-annihilation. When the microwave radiation is switched on after a delay of 510 ns, population is transferred to the $2\,^3P_2$ level (dashed red curve). The rate of population transfer to this intermediate level is governed by the resonant Rabi frequency associated with the $2\,^3S_1(0) \rightarrow 2\,^3P_2(0)$ transition. For reference, in a microwave field with an amplitude of 30 V/m, this resonant Rabi frequency is 1.9 MHz. However, because of the short fluorescence lifetime of the $2\,^3P_2$ level, population transferred to this state rapidly decays to the $1\,^3S_1$ ground level (continuous blue curve). At the end of the calculation, the final population of the ground level is taken to represent the change in the annihilation signal monitored in the experiments to obtain the spectral line shape. Note that in Fig. 5(b) the ground-state population grows in time because the $1\,^3S_1$
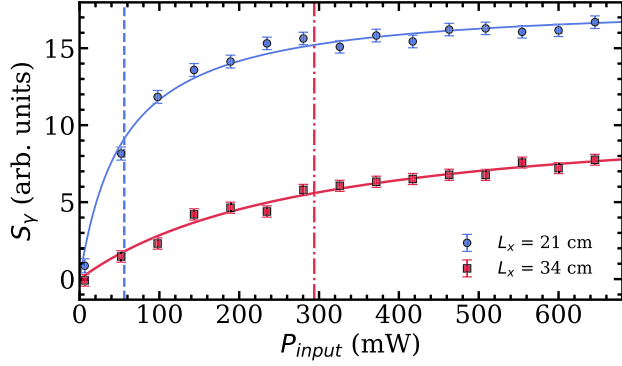
FIG. 6. Measurements of the signal parameter S_γ for the ν_2 transition obtained for $L_x = 21$ cm (blue circles) and $L_x = 34$ cm (red squares). The solid lines show fits of the form in Eq. (5) and the vertical dashed (dot-dashed) line indicates the extracted saturation power P_{sat} for $L_x = 21$ cm ($L_x = 34$ cm) as explained in the text.

annihilation decay rate $\gamma_{1S} = (142\,\text{ns})^{-1}$ is not included in the calculation.

IV. RESULTS AND DISCUSSION

Measurements of the signal parameter S_γ for different microwave input power at 8626.71 MHz are shown in Fig. 6. These data were recorded for two different antenna positions, $L_x = 21$ and 34 cm, and an angle $\theta_H = 0°$ with all data presented being the average across three detectors. The data are fitted with the function [52]

$$S_\gamma = a\left[1 - \frac{1}{1 + bP_{\text{input}}}\right], \qquad (5)$$

where a and b are free fit parameters, P_{input} is the microwave power applied to the horn antenna, and the quantity bP_{input} is the saturation parameter [27]. The saturation power can be obtained from this function, where saturation is defined to occur when $bP_{\text{input}} > 1$. From the fits, the parameter b was found to be 0.018 ± 0.001 and 0.0035 ± 0.0005 mW^{-1} for $L_x = 21$ and 34 cm, respectively. Thus, the corresponding saturation powers (P_{sat}) were 56 ± 3 and 294 ± 42 mW, as indicated by the vertical lines in Fig. 6. Moving the horn antenna further away from the vacuum chamber reduces the microwave power transmitted into the MER, and hence also the degree of saturation. However, other than the reduced power there is no significant difference in the measurements performed for the two different positions, which supports the idea that reflections in the vacuum chamber remove the distinction between the near- and far-field regimes.

Figure 7 shows line shapes measured using three microwave power values, recorded for antenna position $L_x = 21$ cm and $\theta_H = 0°$. The corresponding fit parameters obtained are displayed in Fig. 8. The measured values of ν_R show a consistent shift below the theory value [Fig. 8(a)], with the average of the measured transition frequencies being approximately 2 MHz lower than the (Zeeman shifted) theory value.

The linewidths (FWHM) obtained for these measurements are presented in Fig. 8(b), and show increasing widths caused
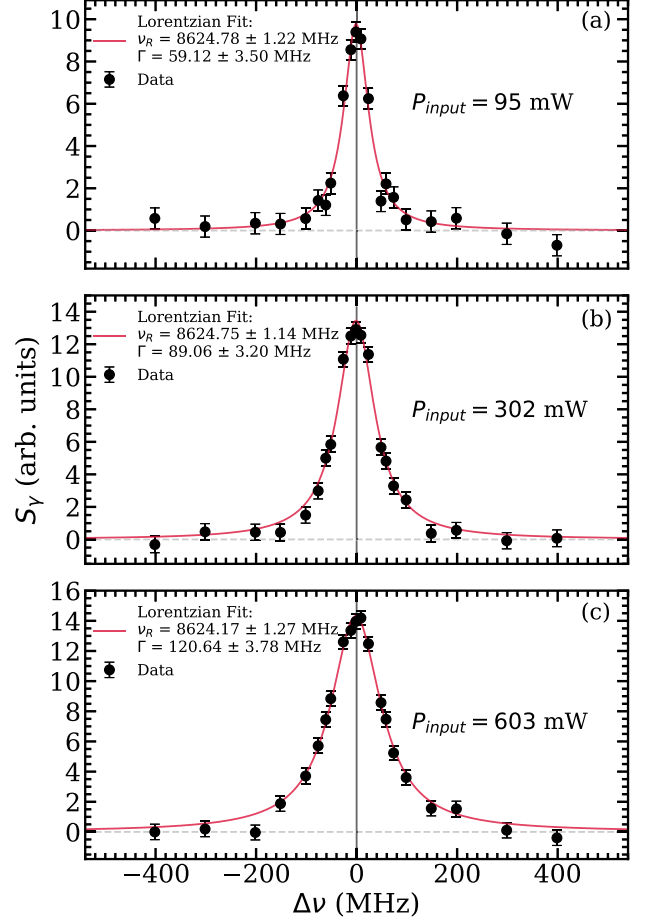

FIG. 7. ν_2 line shapes measured for three P_{input} values, as indicated in the panels, with $L_x = 21$ cm and $\theta_H = 0°$. The solid (red) curves are Lorentzian fits, with the corresponding fit parameters shown in the legends. The solid (gray) vertical line at $\Delta \nu = 0$ corresponds to the Zeeman shifted theoretical transition frequency 8625.84 MHz.

by power broadening. A fit has been made to the data using the function [27]

$$\Gamma = \Gamma_0\sqrt{1 + bP_{\text{input}}}, \qquad (6)$$

where Γ_0 is the width (FWHM) for zero power, and bP_{input} is again the saturation parameter. The fit to these data yields $\Gamma_0 = 45.0 \pm 2.2$ MHz and $b = 0.009 \pm 0.001$ mW^{-1} ($P_{\text{sat}} = 111 \pm 14$ mW). The zero-field width is within 3σ of the theoretical natural linewidth of 50 MHz, and b disagrees with the corresponding saturation measurement of Fig. 6 (i.e., 0.018 ± 0.001 mW^{-1}). This could indicate that increasing the microwave power does not only increase the $2\,^3S_1 \to 2\,^3P_2$ transition rate, but can also increase the number of atoms that are addressed by the radiation field. This would increase both the saturation yield and the linewidth, but not necessarily with the same power dependence. This would also mean that Eqs. (5) and (6) are not strictly valid, which could explain the small deviation of the obtained Γ_0 from 50 MHz. The calculated line shapes also indicate a slightly narrower Γ_0 of 47.3 ± 0.4 MHz.
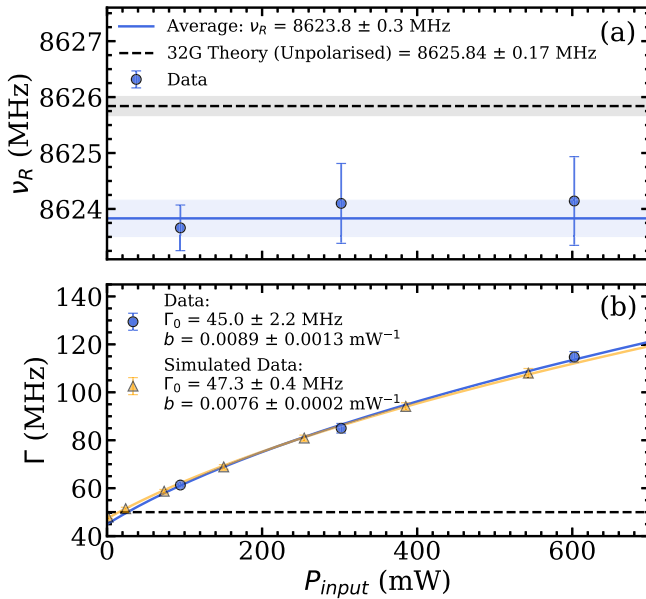
FIG. 8. Lorentzian fit parameters (a) ν_R and (b) Γ obtained from line shapes measured for different microwave power P_{input}. These data were recorded with $L_x = 21$ cm and $\theta_H = 0°$.

Figure 9 shows example line shapes measured for different horn antenna angles, with $L_x = 34$ cm. These measurements show a large shift in the obtained resonance frequency as a function of horn antenna angle. Simulated line shapes for the same parameters are shown in Fig. 10. All results obtained from both simulations and measurements are shown in Fig. 11, including measurements made with $L_x = 21$ cm. These measurements indicate that the linear shift in the transition frequencies for different horn antenna angles is not reproduced by the simulations, although some evidence is found for variations on the order of a few MHz. The simulated data were obtained for the same frequencies as the measurements, with an additional point at $-9.8°$ obtained as a sensitivity test. The horizontal error bars for the simulated data represent the fact that the absolute horn orientation with respect to the vacuum chamber is not known to better than $\approx 2°$.

In a measurement in which the radiation propagates as a focused beam with a well-defined direction of propagation, such shifts could arise via Doppler effects. In the present case this cannot explain the observations because (1) microwave reflections in the vacuum chamber mean that there is not a well-defined direction for the radiation propagation and (2) even if the most extreme atom-radiation interactions are considered the magnitude of the effect and its angular dependence are much too large.

The former is apparent from the radiation patterns shown in Fig. 3, which clearly indicate that there is a complicated radiation field in and around the vacuum chamber, and that the directionality of the microwave radiation is therefore not well defined. The latter is evident from the Ps velocity distributions, where the *maximum* Ps speed v_{Ps} (in any direction) is on the order of 2×10^7 cm/s [28]. Thus $v_{\text{Ps}}/c \lesssim 7 \times 10^{-4}$, and the maximum possible Doppler shift would be ≈ 6 MHz (for the ν_2 transition). However, most atoms are much slower
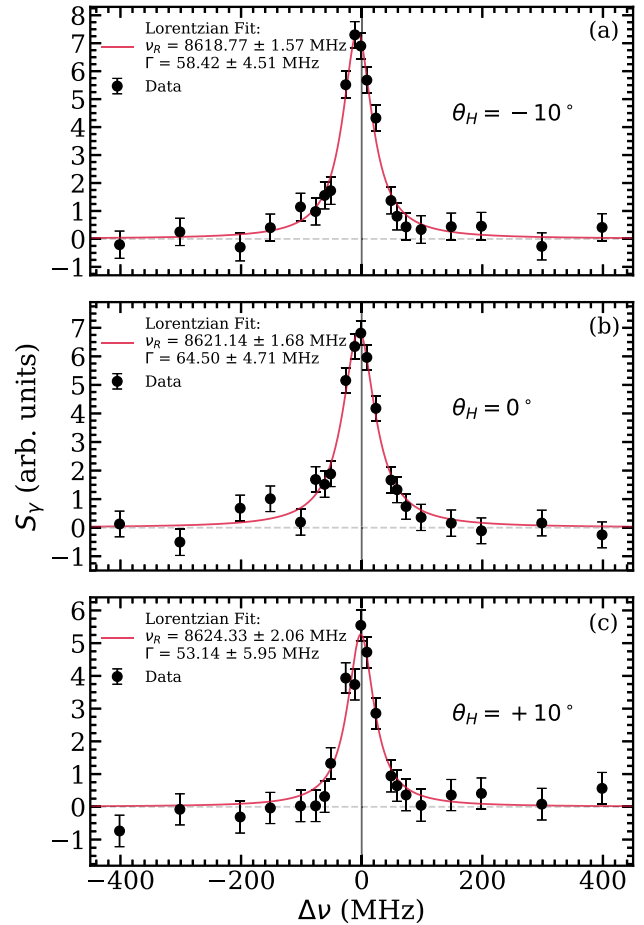

FIG. 9. ν_2 line shapes for three of the measured θ_H values, as indicated in the panels, with $L_x = 34$ cm and $P_{\text{input}} = 300$ mW. The solid (red) curves are Lorentzian fits, with the corresponding fit parameters shown in the legends. The solid (gray) vertical line at $\Delta\nu = 0$ corresponds to the Zeeman shifted theoretical transition frequency 8625.84 MHz.

than this. Furthermore, the high sensitivity of the obtained ν_R frequencies to the horn antenna angle, as evidenced by the data in Fig. 11, is not consistent even with this case, since the variation with angle would depend on $v_{\text{Ps}} \sin(\theta_H)$, giving sub-MHz shifts for a $10°$ rotation. Therefore, Doppler shifts cannot explain the observed strong dependence of ν_R on the angular orientation of the horn antenna.

Previously identified systematic effects, including ac Stark shifts, quantum interference, second-order Doppler shifts, motional Stark effects, and stray electric fields, are also likely to contribute only at the sub-MHz level [27,28], and in general these would not depend on the horn antenna angle.

As discussed in Sec. II B, asymmetric Lorentz functions were used to characterize the degree of asymmetry in the measured data. The asymmetric Lorentz function was fitted to the line shapes used to obtain the $L_x = 34$ data shown in Fig. 11, and the resulting q_L and ν_R values are shown in Figs. 12(a) and 12(b), respectively, along with the corresponding parameters obtained from the line-shape simulations.

The average of the asymmetry parameters for measurements performed using a horn antenna position $L_x = 34$ cm
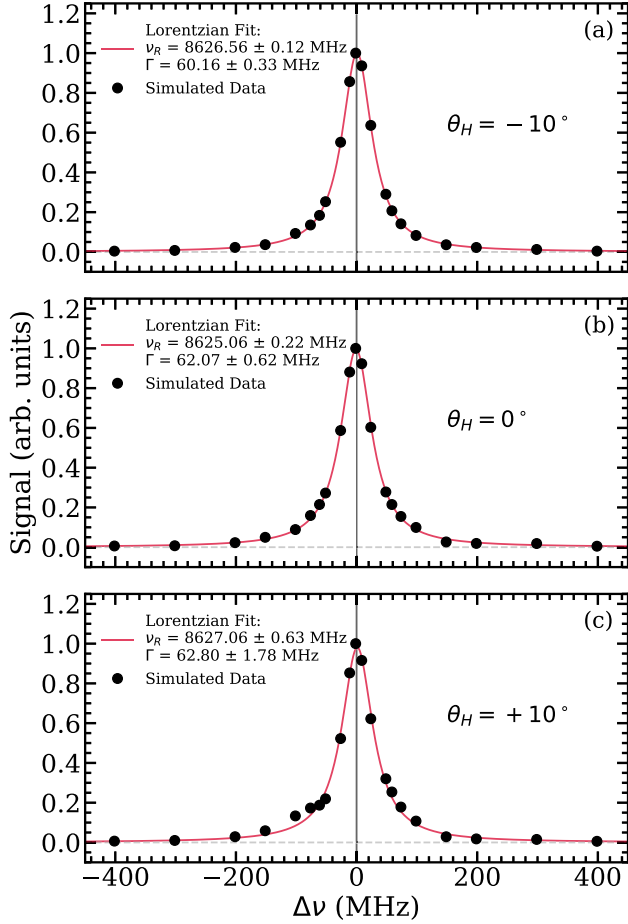
FIG. 10. Simulated line shapes for conditions corresponding to those shown in Fig. 9. The simulations were obtained using 500 particle trajectories.
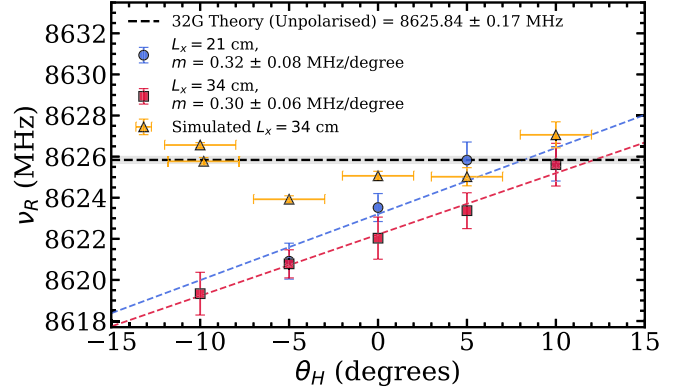

FIG. 11. Measured transition frequencies for different θ_H values for both $L_x = 21$ cm (blue circles) and $L_x = 34$ cm (red squares) with corresponding linear fits (dashed lines). P_{input} was set to 95 mW (300 mW) at $L_x = 21$ cm (34 cm) to match the observed power broadening. Simulated line-shape data obtained using the process described in Sec. III for $L_x = 34$ cm are also shown (yellow triangles).

exhibit relatively large shifts (i.e., MHz level) without also exhibiting large asymmetries, and this therefore probably also applies to the previous ν_0 measurements [10]. For a conclusive assessment of the extent to which lines might be shifted, better quality data will be required, such that smaller asymmetries can be unambiguously resolved. Moreover, at the $\approx$100-kHz level of precision, the line shapes will in fact be asymmetric due to quantum interference effects (see [28] for details), and

and power $P_{\mathrm{input}} = 300$ mW is shown in Fig. 12(a). The obtained q_L parameter is nonzero; however, it is close to zero (within two standard deviations). This suggests that the line shapes are not significantly asymmetric. However, the significance of any asymmetry present is in part related to the error bars on the experimental data; small asymmetries cannot be detected if the resulting line distortions are much smaller than the statistical variations in the data. Asymmetries in the present data can be considered to be insignificant insofar as the symmetric and asymmetric functions both yield the same resonance frequency (within error bars).

Taking into account all measurements performed (i.e., line shapes measured for all microwave powers and horn antenna positions), the average value of q_L was found to be -0.54 ± 0.56 GHz^{-1}, and the average value of q_L obtained from the line-shape simulations was $q_L = 1.7 \pm 0.1$ GHz^{-1}. By comparison, fitting the asymmetric Lorentzian function to the previously measured ν_2 waveguide line shapes [27] yields an average value of $q_L = -23.2 \pm 0.5$ GHz^{-1}.

It is important to remember that agreement between symmetric and asymmetric fits may not be taken as an indication that the underlying data are not actually asymmetric, and thus does not necessarily mean that the lines are not shifted. As is shown, both measurements and simulations (see Fig. 11) may
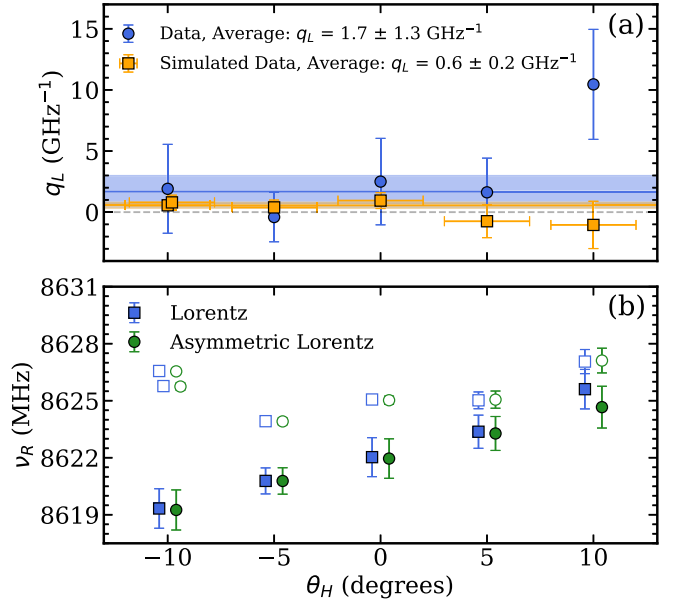

FIG. 12. (a) q_L and (b) ν_R values for different horn antenna angles for both measured and simulated line shapes. The average value of the measured (simulated) q_L values is indicated by the blue (orange) band in (a). The measured ν_R values in (b) are shown for fits using both symmetric (blue filled squares) and asymmetric (blue filled circles) Lorentz functions as discussed in the text. The corresponding simulated data are shown as unfilled symbols. These data were recorded or simulated using a horn antenna position $L_x = 34$ cm and power $P_{\mathrm{input}} = 300$ mW.

this would then have to be explicitly taken into account in line-shape modeling. Because of the broad natural linewidth, this may prove to be a limiting factor for Ps $n = 2$ fine-structure measurements performed using the methodology described here.

The data shown in Fig. 11 indicate that the measured ν_R frequencies have a linear variation of ≈ 300 kHz/deg. Changing the horn antenna angle will also change the location at which transitions will occur, and therefore the Zeeman shift will also vary, but the magnetic-field variations (see Fig. 4) would give rise to sub-MHz shifts. As shown in Fig. 11, the line-shape simulations described in Sec. II B do not exhibit the same dependence with the horn antenna angle. There is a smaller effect which could indicate that some aspects of the microwave field simulations shown in Fig. 3 do not perfectly reproduce the experimental conditions, such as variations in the reflectivity of the internal surfaces caused by contamination or surface imperfections, welding features, and so on. Nevertheless, a MHz scale shift is reproduced in the simulations, and it is therefore reasonable to conclude that the observed shifts are caused by small line-shape distortions arising from the variations in the microwave radiation field distributions.

V. CONCLUSIONS

A horn antenna has been used as a source of free-space microwave radiation at a frequency of ≈ 8.6 GHz that is capable of saturating the $2\,^3S_1 \rightarrow 2\,^3P_2$ transition in positronium. Measurements of the spectral line shape of this transition were performed yielding Lorentzian line shapes with no significant asymmetry. However, the apparent transition frequencies were found to depend strongly on the orientation of the horn antenna with respect to the vacuum chamber in which the Ps atoms were produced. The observed shifts are inconsistent with Doppler shifts, or any other previously identified systematic effects.

Numerical simulations of the microwave radiation field within the experimental apparatus indicate that multiple reflections lead to complex microwave radiation field distributions. Similar effects were also previously found in numerical simulations of the ν_J transitions in waveguides, in that case resulting in both line-shape distortions and shifts [28]. In this paper, line-shape calculations using the radiation field and particle trajectory simulations do not exactly reproduce the observed linear shift in transition frequency with the horn antenna angle, but do indicate that field-dependent shifts can occur without asymmetric line shapes (see Fig. 11).

Thus, the measurements and simulations presented here show that large (apparent) shifts can arise by varying the distribution of the radiation fields, but that this does not necessarily result in measurably asymmetric line shapes. Therefore, the previously observed asymmetries and shifts [10,27] can be qualitatively explained by this effect. These results suggest that suitable modifications of the vacuum chamber in which waveguides are used should significantly reduce or eliminate reflections, resulting in well-defined fields and making it possible to perform precision spectroscopy without complications from these effects.

[1] J. A. Wheeler, Polyelectrons, Ann. N. Y. Acad. Sci. **48**, 219 (1946).

[2] S. G Karshenboim, Precision study of positronium: Testing bound state QED theory, Int. J. Mod. Phys. A **19**, 3879 (2004).

[3] G. S. Adkins, D. B. Cassidy, and J. Pérez-Ríos, Precision spectroscopy of positronium: Testing bound-state QED theory and the search for physics beyond the standard model, Phys. Rep. **975**, 1 (2022).

[4] M. S. Fee, S. Chu, A. P. Mills, Jr., R. J. Chichester, D. M. Zuckerman, E. D. Shaw, and K. Danzmann, Measurement of the positronium $1\,^3S_1$-$2\,^3S_1$ interval by continuous-wave two-photon excitation, Phys. Rev. A **48**, 192 (1993).

[5] A. P. Mills, Jr. and G. H. Bearman, New Measurement of the Positronium Hyperfine Interval, Phys. Rev. Lett. **34**, 246 (1975).

[6] A. P. Mills, Jr., S. Berko, and K. F. Canter, Fine-Structure Measurement in the First Excited State of Positronium, Phys. Rev. Lett. **34**, 1541 (1975).

[7] M. W. Ritter, P. O. Egan, V. W. Hughes, and K. A. Woodle, Precision determination of the hyperfine-structure interval in the ground state of positronium. V, Phys. Rev. A **30**, 1331 (1984).

[8] S. Hatamian, R. S. Conti, and A. Rich, Measurements of the 2^3S_1-2^3P_J ($J = 0, 1, 2$) Fine-Structure Splittings in Positronium, Phys. Rev. Lett. **58**, 1833 (1987).

[9] D. Hagena, R. Ley, D. Weil, G. Werth, W. Arnold, and H. Schneider, Precise Measurement of $n = 2$ Positronium Fine-Structure Intervals, Phys. Rev. Lett. **71**, 2887 (1993).

[10] L. Gurung, T. J. Babij, S. D. Hogan, and D. B. Cassidy, Precision Microwave Spectroscopy of the Positronium $n = 2$ Fine Structure, Phys. Rev. Lett. **125**, 073002 (2020).

[11] Andrzej Czarnecki, Kirill Melnikov, and Alexander Yelkhovsky, Positronium S-state spectrum: Analytic results at $O(m\alpha^6)$, Phys. Rev. A **59**, 4316 (1999).

[12] Andrzej Czarnecki, Kirill Melnikov, and Alexander Yelkhovsky, Positronium Hyperfine Splitting: Analytical Value at $O(m\alpha^6)$, Phys. Rev. Lett. **82**, 311 (1999).

[13] G S Adkins, Higher order corrections to positronium energy levels, J. Phys.: Conf. Ser. **1138**, 012005 (2018).

[14] M. I. Eides and V. A. Shelyuto, Three-loop corrections to lamb shift in positronium: Electron factor and polarization, Phys. Lett. B **832**, 137247 (2022).

[15] J. P. Gordon, H. J. Zeiger, and C. H. Townes, The maser—New type of microwave amplifier, frequency standard, and spectrometer, Phys. Rev. **99**, 1264 (1955).

[16] J. P. Gordon, H. J. Zeiger, and C. H. Townes, Molecular microwave oscillator and new hyperfine structure in the microwave spectrum of NH_3, Phys. Rev. **95**, 282 (1954).

[17] A. L. Schawlow and C. H. Townes, Infrared and optical masers, Phys. Rev. **112**, 1940 (1958).

[18] C.H. Townes and A.L. Schawlow, *Microwave Spectroscopy*, Dover Books on Physics (Dover, New York, 1975).

[19] W. E. Lamb and R. C. Retherford, Fine structure of the hydrogen atom by a microwave method, Phys. Rev. **72**, 241 (1947).

[20] H. A. Bethe, The electromagnetic shift of energy levels, Phys. Rev. **72**, 339 (1947).

[21] W. E. Lamb and R. C. Retherford, Fine structure of the hydrogen atom. Part I, Phys. Rev. **79**, 549 (1950).

[22] C. W. Fabjan and F. M. Pipkin, Resonance-narrowed-lamb-shift measurement in hydrogen, $n = 3$, Phys. Rev. A **6**, 556 (1972).

[23] S. R. Lundeen and F. M. Pipkin, Measurement of the Lamb Shift in Hydrogen, $n = 2$, Phys. Rev. Lett. **46**, 232 (1981).

[24] S. R. Lundeen and F. M. Pipkin, Separated oscillatory field measurement of the lamb shift in H, $N = 2$, Metrologia **22**, 9 (1986).

[25] N. Bezginov, T. Valdez, M. Horbatsch, A. Marsman, A. C. Vutha, and E. A. Hessels, A measurement of the atomic hydrogen Lamb shift and the proton charge radius, Science **365**, 1007 (2019).

[26] N. F. Ramsey, Experiments with separated oscillatory fields and hydrogen masers, Rev. Mod. Phys. **62**, 541 (1990).

[27] L. Gurung, T. J. Babij, J. Pérez-Ríos, S. D. Hogan, and D. B. Cassidy, Observation of asymmetric line shapes in precision microwave spectroscopy of the positronium $2\,^3S_1 \rightarrow 2\,^3P_J$ ($J = 1, 2$) fine-structure intervals, Phys. Rev. A **103**, 042805 (2021).

[28] L. A. Akopyan, T. J. Babij, K. Lakhmanskiy, D. B. Cassidy, and A. Matveev, Line-shape modeling in microwave spectroscopy of the positronium $n = 2$ fine-structure intervals, Phys. Rev. A **104**, 062810 (2021).

[29] B. S. Cooper, A. M. Alonso, A. Deller, T. E. Wall, and D. B. Cassidy, A trap-based pulsed positron beam optimised for positronium laser spectroscopy, Rev. Sci. Instrum. **86**, 103101 (2015).

[30] D. B. Cassidy, Experimental progress in positronium laser physics, Euro. Phys. J. D **72**, 53 (2018).

[31] A. P. Mills, Jr. and E. M. Gullikson, Solid neon moderator for producing slow positrons, Appl. Phys. Lett. **49**, 1121 (1986).

[32] J. R. Danielson, D. H. E. Dubin, R. G. Greaves, and C. M. Surko, Plasma and trap-based techniques for science with positrons, Rev. Mod. Phys. **87**, 247 (2015).

[33] A. P. Mills, Jr., Time bunching of slow positrons for annihilation lifetime and pulsed laser photon absorption experiments, Appl. Phys. **22**, 273 (1980).

[34] L. Liszkay, C. Corbel, P. Perez, P. Desgardin, M. F. Barthe, T. Ohdaira, R. Suzuki, P. Crivelli, U. Gendotti, A. Rubbia, M. Etienne, and A. Walcarius, Positronium reemission yield from mesostructured silica films, Appl. Phys. Lett. **92**, 063114 (2008).

[35] D. B. Cassidy, P. Crivelli, T. H. Hisakado, L. Liszkay, V. E. Meligne, P. Perez, H. W. K. Tom, and A. P. Mills, Jr., Positronium cooling in porous silica measured via Doppler spectroscopy, Phys. Rev. A **81**, 012715 (2010).

[36] A. Deller, B. S. Cooper, T. E. Wall, and D. B. Cassidy, Positronium emission from mesoporous silica studied by laser-enhanced time-of-flight spectroscopy, New J. Phys. **17**, 043059 (2015).

[37] A. M. Alonso, B. S. Cooper, A. Deller, S. D. Hogan, and D. B. Cassidy, Controlling Positronium Annihilation with Electric Fields, Phys. Rev. Lett. **115**, 183401 (2015).

[38] A. M. Alonso, S. D. Hogan, and D. B. Cassidy, Production of $2\,^3S_1$ positronium atoms by single-photon excitation in an electric field, Phys. Rev. A **95**, 033408 (2017).

[39] John Volakis, *Antenna Engineering Handbook*, 4th ed. (McGraw-Hill, New York, 2007).

[40] D. B. Cassidy, S. H. M. Deng, H. K. M. Tanaka, and A. P. Mills, Jr., Single shot positron annihilation lifetime spectroscopy, Appl. Phys. Lett. **88**, 194105 (2006).

[41] A. M. Alonso, B. S. Cooper, A. Deller, and D. B. Cassidy, Single-shot positron annihilation lifetime spectroscopy with LYSO scintillators, Nucl. Instrum. Methods Phys. Res., Sect. A **828**, 163 (2016).

[42] A. M. Alonso, B. S. Cooper, A. Deller, S. D. Hogan, and D. B. Cassidy, Positronium decay from n = 2 states in electric and magnetic fields, Phys. Rev. A **93**, 012506 (2016).

[43] U. Fano, Effects of configuration interaction on intensities and phase shifts, Phys. Rev. **124**, 1866 (1961).

[44] A. L. Stancik and E. B. Brauns, A simple asymmetric lineshape for fitting infrared absorption spectra, Vib. Spectros. **47**, 66 (2008).

[45] CST Studio Suite, Dassault Systemes, https://www.3ds.com/products-services/simulia/products/cst-studio-suite/.

[46] M. Charlton and J. W. Humberston, *Positron Physics*, 1st ed., Cambridge Monographs on Atomic, Molecular, and Chemical Physics Vol. 2 (Cambridge University, Cambridge, England, 2001).

[47] M. H. Weber, S. Tang, S. Berko, B. L. Brown, K. F. Canter, K. G. Lynn, A. P. Mills, L. O. Roellig, and A. J. Viescas, Observation of Positronium Specular Reflection from LiF, Phys. Rev. Lett. **61**, 2542 (1988).

[48] G. Lindblad, On the generators of quantum dynamical semigroups, Commun. Math. Phys. **48**, 119 (1976).

[49] V. Gorini, A. Kossakowski, and E. C. G. Sudarshan, Completely positive dynamical semigroups of n-level systems, J. Math. Phys. **17**, 821 (1976).

[50] J. R. Johansson, P. D. Nation, and F. Nori, Qutip: An open-source python framework for the dynamics of open quantum systems, Comput. Phys. Commun. **183**, 1760 (2012).

[51] J. R. Johansson, P. D. Nation, and F. Nori, Qutip 2: A python framework for the dynamics of open quantum systems, Comput. Phys. Commun. **184**, 1234 (2013).

[52] C. J. Foot, *Atomic Physics*, Oxford Master Series in Physics (Oxford University, New York, 2005).